Journal of The Electrochemical Society, 2023 **170** 064506

Catalytic Activity and Stability of Non-Platinum Group Metal Oxides for the Oxygen Evolution Reaction in Anion Exchange Membrane Electrolyzers

Emily K. Volk,[1] Stephanie Kwon,[1,2,z] and Shaun M. Alia[1,3,z]

[1]*Advanced Energy Systems Graduate Program, Colorado School of Mines, Golden Colorado 80401, United States of America*
[2]*Department of Chemical and Biological Engineering, Colorado School of Mines, Golden, Colorado 80401, United States of America*
[3]*Chemistry and Nanoscience Center, National Renewable Energy Laboratory, Golden, Colorado 80401, United States of America*

The activities and stabilities of non-platinum group metals (PGMs) in the forms of monometallic (Mn_2O_3, Fe_2O_3, Co_3O_4, NiO) and bimetallic ($NiFe_2O_4$, $CoNiO_2$) oxides were assessed for the oxygen evolution reaction (OER) in alkaline media and compared with IrO_2. Both half-cell, rotating disc electrode (RDE) apparatus and single-cell, membrane electrode assemblies (MEA) were used to study kinetic and device-level performance in parallel and to provide insights into the use of these materials in anion exchange membrane (AEM) electrolyzers. Normalization of RDE results by geometric and physical surface areas, double layer capacitance, and metal content probed differences in physically vs electrochemically accessible surface areas and ensured reported trends were independent of the normalization method. The results showed that: (i) Ni- and Co- containing materials met or exceeded IrO_2 performance in both RDE and MEA testing, (ii) Co_3O_4 deactivated over time-on-stream (1.8 V for 13.5 h) due to oxide and, relatedly, particle growth, (iii) $NiFe_2O_4$ increased in activity over time-on-stream due to dissolution of Fe and an increased Ni/Fe ratio, and (iv) reduction of catalyst layer resistance is an avenue to further increase device-level performance. These results demonstrated the clear viability for non-PGMs to be used as anode catalysts in AEM devices.
 [DOI: 10.1149/1945-7111/acd605]

Manuscript submitted December 9, 2022; revised manuscript received April 5, 2023. Published June 16, 2023.

Supplementary material for this article is available online

Electrochemical H_2 production via low-temperature H_2O electrolysis is a promising strategy to facilitate decarbonization across sectors including transportation; steel, ammonia, and cement production; and chemical synthesis.[1,2] Electricity cost reductions concurrent with an increase in wind and solar power on the grid have made the production of green H_2 at scale more feasible and sustainable.[3] However, current state-of-the-art proton exchange membrane (PEM) electrolyzers require the use of expensive and rare platinum group metals (PGMs) for catalysts and hardware, limiting scale-up feasibility.[3–5] Iridium (Ir) is almost exclusively used for the O_2 evolution reaction (OER) at the anode in PEM electrolyzers,[3,4] as non-PGM alternatives will oxidize into soluble forms at the low pH and high potential operating conditions of these systems.[6] The development of electrolyzers that can operate with inexpensive, non-PGM materials while meeting or exceeding the performance of PEM electrolyzers is thus highly desired to achieve H_2 at scale.

Recently, anion exchange membrane (AEM) electrolyzers have emerged as an alternative strategy to achieve such a goal by combining the benefits of traditional liquid alkaline systems and current high-performing PEM electrolyzers. Specifically, AEM systems utilize the same zero-gap approach as PEM electrolyzers to achieve low ohmic losses and high operating current densities ($\sim$1 A cm^{-2} at 1.8 V).[4,7] Furthermore, many non-PGMs are thermodynamically stable in solid oxide or hydroxide forms at high pH and high potentials; the near-surface alkaline environment in AEM systems thus allows for the use of non-PGM materials for catalysts, porous transport layers, flow fields, and separator coatings.[6] AEM development has been historically limited by membrane technology,[8–10] but recent advancements have resulted in significant improvements to both performance and durability,[7,11–14] thereby increasing the need for the development of other components including electrocatalysts for the H_2 evolution reaction (HER) (at the cathode) and OER (at the anode). This work will focus on assessing commercially available catalysts for OER, which imposes larger overpotentials in electrochemical H_2O splitting than HER, with a goal of proposing viable non-PGM anode catalysts that can replace current Ir-based catalysts.

Past research efforts have demonstrated that metallic Co and Ni in polycrystalline film[15] and nanoparticulate morphologies[16] have overpotentials for alkaline OER comparable to those of Ir, revealing the viability of non-PGMs as candidates for OER in alkaline media. These non-PGM metals, however, convert into their thermodynamically-favored, oxidized forms under operating conditions,[6] raising questions about their active chemical states, which may change during testing. Among studies that instead evaluated metal oxides as starting materials, many contradicting performance trends have been reported, with oxide forms of Co,[17–19] Ni,[20–22] and NiFe[16,23–25] all having been suggested as the best performing non-PGM material. These controversies are at least in part due to differences in testing conditions, the chemical states and crystalline structures of the tested oxides, and the normalization methods used. Electrochemical testing conditions can vary in the choice of electrolyte and its concentration (which can affect double-layer structure and ion transport within the system) and in the chosen applied voltage ranges (which directly affect observed current densities, overpotentials, and kinetic rate constants). Metal oxides in different oxidation states and crystalline phases have been tested in literature, including thin-film layered (oxy)hydroxides[22–25] and oxides in the forms of rutile, spinel, and perovskite structures.[16,17,21] Some previous reports have also used electrochemically oxidized metal electrodes,[20] which makes it difficult to assess their relevant chemical states and crystalline phases. Furthermore, differences in surface area and electrical conductivity can contribute to differences in measured activity among different oxides of the same element, highlighting the importance of accurate normalization methods. Yet, previous studies often normalize the current density by the geometric surface area of the electrode, making a rigorous comparison across studies difficult and leading to controversial conclusions. Finally, in identifying

[z]E-mail: kwon@mines.edu; shaun.alia@nrel.gov

materials as replacements for PGM catalysts in AEM systems, it is vital to assess catalyst stability at operating conditions, device-level integrability and activity, and scale-up viability, considerations that have rarely been considered in previous studies.

This study seeks to provide baseline testing of monometallic and bimetallic oxides of first-row transition metals (Mn, Fe, Co, and Ni) and compare results to the current PEM state-of-the-art OER catalyst, IrO_2.[26,27] Specifically, this work aims to fill knowledge gaps in literature via evaluation of commercially available, fully oxidized, non-PGM nanoparticles for (i) their OER activities in alkaline environments (normalized by the geometric surface area of the electrode, the physical surface area of the catalysts, the double layer capacitance, and the mass loading of metals in the catalysts), (ii) their stability at operating conditions by comparing activity (current at 1.65 V) before and after stress testing at high potential (1.8 V; 13.5 h) and iii) their performance at the device level via single-cell, membrane electrode assembly (MEA) experiments. The results showed that Co_3O_4 provided the highest OER activity (across all normalization methods) among all non-PGM catalysts tested and exceeded the activity of IrO_2 for all normalization methods except by physical surface area. Co_3O_4 catalysts, however, deactivated over time-on-stream at operating conditions. Furthermore, Co has been identified as having high material criticality,[5,28–31] rendering Co_3O_4 a less-feasible candidate for IrO_2 replacement. Alternatively, Ni-containing catalysts, such as $NiFe_2O_4$, met or exceeded IrO_2 OER activity across most normalization methods (except by physical surface area) and typically have low material criticality relative to Co or Ir.[28,31] $NiFe_2O_4$ performance improved over time-on-stream due to an increased Ni/Fe ratio caused by dissolution of Fe, and, at the device level, this material achieved current densities of $> 1\ A\ cm^{-2}$ at 1.8 V, exceeding the performance of IrO_2. These results reveal the strong viability of Ni-containing oxides for operation in AEM electrolyzers, offering new perspectives on their use as PGM replacements in terms of activity, stability, and performance at the device level.

Experimental

Catalyst materials.—Catalyst materials were obtained from commercial suppliers and used without further treatment. *PGM baseline:* IrO_2 (Alfa Aesar, 99.99%); *non-PGM monometallic oxides:* Mn_2O_3 (US Research Nanomaterials Inc., 99.2%), γ-Fe_2O_3 (US Research Nanomaterials Inc., 99%), Co_3O_4 from two suppliers (US Research Nanomaterials Inc., 99%; Particular Materials, no purity provided), NiO (US Research Nanomaterials Inc., 99%); *non-PGM bimetallic oxides:* $NiFe_2O_4$ from three suppliers (US Research Nanomaterials Inc., 98%; Nanografi, 98.99%; Sigma Aldrich, ⩾98%), $CoNiO_2$ (US Research Nanomaterials Inc., 99.9%); *cathode catalyst:* Pt on C support (47% Pt, Tanaka Kikinzoku Kogyo, TEC10E50E).

Characterizations of physical and electrochemical properties of catalysts.—X-ray diffractograms (XRD) were obtained ($2\theta = 13.5°$ –88°) using a Bruker D8 Discover with Cu K-α radiation ($\lambda = 1.5406$) and GADDS XRD system. Crystalline sizes were determined from the XRD patterns using Bragg's Law and the Scherrer equation.[32] The Brunauer-Emmet-Teller (BET) surface area[33] of each screened catalyst was determined from N_2 physisorption isotherms (at 77 K) measured using a Quantachrome Autosorb iQ. The double layer capacitance was estimated from cyclic voltammograms collected in the non-Faradaic region (0–0.6 or 0–0.3 V) at scan rates of 100, 50, 20, and 10 mV s^{-1} and used as a proxy for the electrochemically active surface area[34] (details on this method are included in Section S1 of the Supporting Information (SI)).

Formulation of catalyst ink solutions and deposition on electrodes.—Ink solutions for rotating disc electrode (RDE) testing were formulated to target a catalyst loading of 17.8 $\mu g_M\ cm^{-2}$ on the electrode and an ionomer loading of 0.1 $\mu g_{Nafion^®}\ mg_{cat}^{-2}$, following procedures reported in literature.[35,36] Specifically, measured quantities of the oxide catalysts were dispersed in a solution consisting of 76 vol% deionized (DI) water (Milli-Q; ⩾18.2 mΩ resistance and <5 ppb organic carbon content) and 24 vol% of n-propanol (Sigma Aldrich, OmniSolv, HPLC Grade); tables including full ink RDE formulations are included in the SI (Tables SI–SIII, SI). This solution was placed in an ice bath for at least 300 s before the ionomer was added. This mixture was then bath sonicated (900 s), horn sonicated (45 s), and bath sonicated again (2100 s), all in ice. Additional horn sonication was performed as needed before deposition onto the electrode. Prepared inks (10 μL) were deposited onto hand-polished (Alumina MicroPolish, 0.3 μm, Buehler, 40–6363–006) Au RDE working electrodes rotating at 100 RPM. The rotation speed was increased to 500–700 RPM for drying; the optimal rotation speed for drying varied amongst metal oxides and was selected based on the most-uniform coverage achieved, determined visually.

Anode inks for MEA testing were formulated to target 0.5 $mg_{cat}\ cm^{-2}$ and 30 wt% ionomer/catalyst (Versogen, PiperION-A TP-85, 5 wt% in ethanol) in a solution consisting of 10 vol% DI water and 90 vol% n-propanol. Cathode inks were formulated to target 0.3 $mg_{cat}\ cm^{-2}$ and 30 wt% ionomer/catalyst (also PiperION-A TP-85 from Versogen) in a solution containing 57 vol% DI water, and 43 vol% n-propanol; full ink formulations are listed in Tables SIV and SV, SI. Differences in ink formulations between RDE and MEA are related to differences in deposition methods, as described in previous works.[12,35] Anode inks were airbrush sprayed directly onto

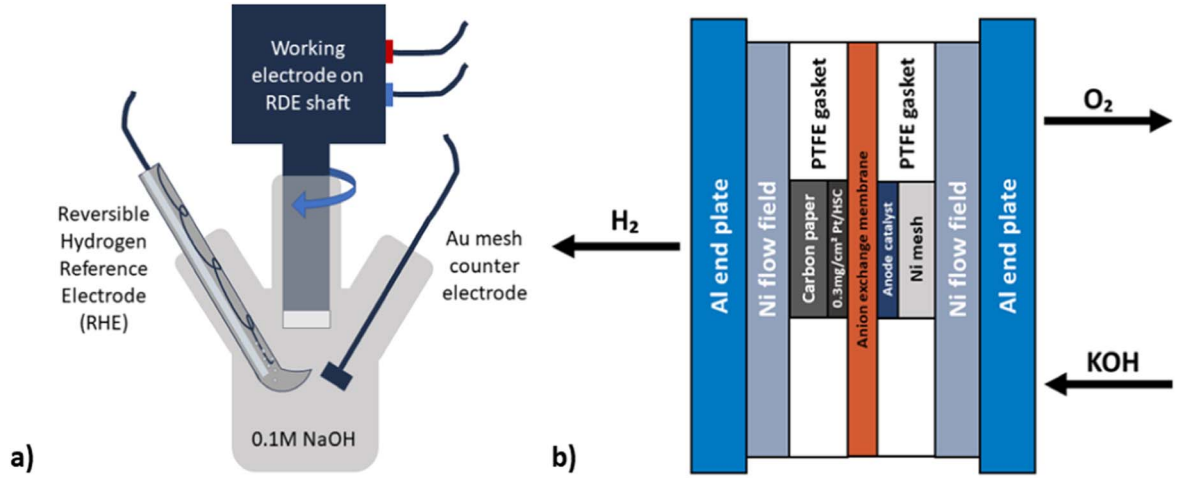

Figure 1. Experimental setups for (a) RDE testing and (b) MEA experiments.

the Ni porous transport layers (PTL; mounted to a vacuum hot plate, 80 °C). Cathode inks were sprayed directly onto the membranes (mounted to a vacuum hot plate, 80 °C) using a Sonotek spray station with Accumist nozzle. Anode and cathode catalyst loadings were confirmed with X-ray fluorescence (XRF; measurements taken 3x at 30 s exposures on a Fischer XDV-SDD XRF).

Rotating disc electrode (RDE) tests.—All RDE tests were conducted at ambient temperature (23 °C) in 170 ml of 0.1 M sodium hydroxide (NaOH) electrolyte (Sigma-Aldrich, TraceSELECT grade, 99.9995%), bubbled with N_2 (⩾300 s) to remove dissolved O_2. A glass, three-electrode cell was used (Fig. 1a), which included a catalyst-coated Au RDE working electrode (0.196 cm^2, Pine Research Instrumentation, AFE5T050AU), Au wire/mesh counter electrode, and reversible hydrogen reference electrode (RHE). The working electrode speed was controlled by a modulated speed rotator (Pine Research Instrumentation, AFMSRCE) and electrochemical measurements were performed using an Autolab PGSTAT302N potentiostat (Eco Chemie, Metrohm Autolab). Linear sweep voltammetry was used to determine catalyst activity; these tests were preceded by five cycles of cyclic voltammetry from 1.2 to 1.8 V (to condition and break-in the catalyst) and were obtained between 1.2 and 2.0 V (scan rate: 20 mV s^{-1}, RDE rotation rate: 2500 revolutions per minute (RPM)). All RDE results were corrected for ohmic (iR) drop through the electrolyte using values obtained from a current interrupter (1.65 V) which was built into the Autolab potentiostat; this correction was performed during the measurement and not during post-processing. All reported voltages are vs RHE. Atmospheric pressure at the experiment site (Golden CO) was assumed to be 82.2 kPa based on an elevation of 1730 m; changes to the thermodynamic cell potential based on this pressure difference from standard conditions (101.3 kPa) were determined and are discussed in Section S4 of the SI.

To assess catalytic stabilities, catalyst activities at 1.65 V were measured before and after a 13.5 h hold at 1.8 V. Prior to post-test data collection, (i) the used electrolyte was stirred, and 15 ml were extracted for inductively coupled plasma mass spectrometry (ICP-MS) analysis (Thermo Scientific, iCAP-Q ICP-MS), (ii) the electrolyte was refreshed and saturated with N_2, and (iii) the electrodes were gently rinsed with DI water and allowed to dry to remove any trapped O_2.[37]

Membrane electrode assembly tests.—IrO_2, Mn_2O_3, Co_3O_4, and $NiFe_2O_4$ catalysts were tested in single-cell, membrane electrode assemblies (MEA) which each had an active area of 5 cm^2 (Fig. 1b). Specifically, the MEAs used consisted of carbon paper gas diffusion layers (Fuel Cell Earth, MGL280, 80280–40), Ni PTLs (Bekaert, BEKIPOR 2NI 18–0.25), PTFE gaskets (254 μm; thickness selected to facilitate compression of the MEA of approximately 20%) and PiperION-A TP-85 (Versogen) membranes (thickness = 80 μm). Hardware for these tests consisted of Al endplates (Fuel Cell Technologies), Au current collectors, and Ni triple serpentine flow fields (Fig. 1b). Before testing, membranes were soaked in 3 M potassium hydroxide (KOH; Millipore, Emsure grade) for 48 h (with the solution refreshed once at 24 h), to facilitate ion exchange from carbonate to hydroxide form; membranes were then stored in 0.5 M KOH until use.

All MEA tests were performed in a 1 M KOH supporting electrolyte (at 80 °C) with a flow rate of 50 ml min^{-1} to the anode and no flow to the cathode (to reflect PEM commercial operating conditions where H_2 backpressure is applied).[4] All MEA tests were performed using a two-electrode configuration and reported potentials are cell potentials. The equilibrium cell potential was corrected for the lower atmospheric pressure of the test site (82.2 kPa) and the non-standard temperature (80 °C) using the Nernst equation (Section S4, SI).[38,39] Electrochemical measurements were taken using an Autolab PGSTAT302N potentiostat (Eco Chemie, Metrohm Autolab) and a 20 A booster (Eco Chemie, Metrohm Autolab). For the initial screening, all materials were tested with the following protocol: (1) potentiostatic polarization curve (20 s per voltage) at 1.40 V, 1.45 V, 1.50 V, 1.55 V, 1.60 V, 1.65 V, 1.70 V, 1.80 V, 1.90 V, and 2.00 V, (2) potentiostatic hold at 2 V (for cell

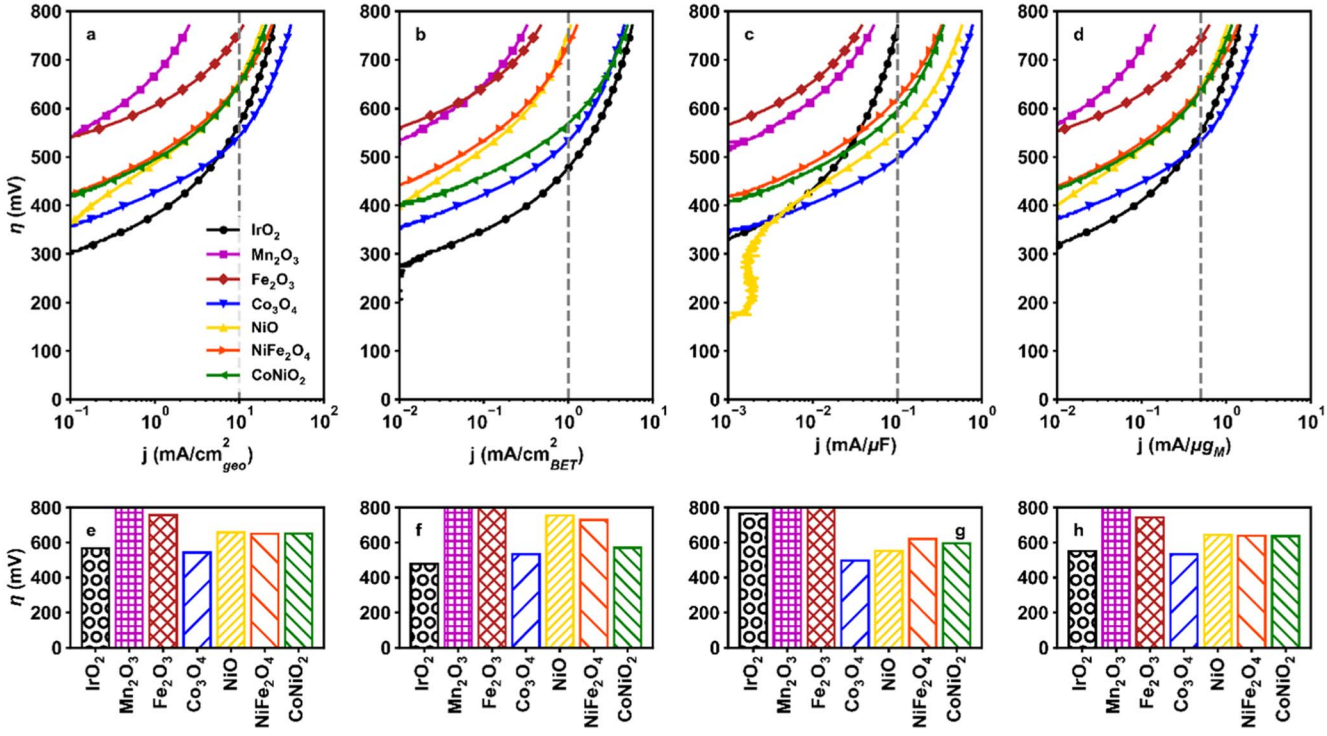

Figure 2. Tafel plots of screened catalysts with current densities normalized by (a) geometric surface areas, (b) BET surface areas, (c) double layer capacitances, (d) mass loadings of metals. Corresponding bar plots show the overpotential at current densities marked by the dashed vertical lines in (a)–(d): (e) 10 mA $cm^{-2}_{geometric}$, (f) 1 mA/cm^2_{BET}, (g) 0.1 mA μF^{-1}, and (h) 1 mA/μg_M. Data were collected at ambient temperature with an RDE rotation rate of 2500 RPM and a scan rate of 20 mV s^{-1}.

conditioning), (3) potentiostatic polarization curve (120 s per voltage) at identical intervals to step 1, (4) Cyclic voltammetry (100 mV s^{-1}, 50 mV s^{-1}, and 20 mV s^{-1}); (5) Electrochemical impedance spectroscopy at 1.25 V and at intervals identical to step 1.

Results and Discussion

Assessments of OER activities based on RDE testing.—RDE measurements were used to screen the OER activities of non-PGM monometallic (Mn_2O_3, Fe_2O_3, Co_3O_4, NiO) and bimetallic ($NiFe_2O_4$, $CoNiO_2$) oxides and compare them to IrO_2 (Fig. 2). The physical and electrochemical properties of the screened oxide catalysts are listed in Table I. RDE measurements minimize interferences from transport limitations of reactants (OH^-) and enable rigorous comparisons among catalysts by separating kinetic ($V < 1.7$ V) and evolved $O_2(g)$ transport limited ($V > 1.8$ V) regimes. Furthermore, due to the low loadings of the catalysts on the RDE tips, we expected minimal interference of catalyst layer microstructure on the transport of $O_2(g)$ products; thus, we approximated measured current densities as being directly proportional to $O_2(g)$ evolution rates. Measured current densities were normalized by four different methods, (i) the geometric surface area of the electrode (where trends are equivalent to those for raw current, as data for all catalysts were divided by the same geometric factor), (ii) the physical surface area (estimated from BET methods), (iii) the double-layer capacitance (determined from cyclic voltammetry), and (iv) the mass loading of metal in each catalyst. The geometric surface area of the electrode is commonly used in literature to normalize current densities,[15,27] although this method does not provide any information on site accessibility. Normalization by the BET surface area accounts for differences in the physically accessible surface area, but does not account for differences in electrochemically active surface areas, nor the type and number of active sites. Rigorous quantification of the electrochemically active surface area requires appropriate probe molecules that adsorb on specific active sites with known stoichiometry; for example, CO stripping methods are widely used for metals such as Pt.[34] However, an appropriate probe molecule has yet to be identified for non-PGM oxides due to difficulties in finding a molecule that selectively and strongly binds to electrochemically active sites for these oxides. Alternative methods include measurement of the double layer capacitance, which approximates the electro-active surface area based on the quantity of charge involved in forming the double layer.[34] This method, however, can have large inherent errors due to the fact that the double-layer capacitance varies with both the catalyst material and the composition of the electrolyte, and cannot be translated to an electrochemically active surface area without the knowledge of the specific capacitance of an ideal, smooth surface of the material of interest obtained in identical electrolyte conditions.[34] As a result, this method can only provide order-of-magnitude comparisons amongst different materials.[15] While developing a more accurate method to quantify electrochemically active sites within metal oxides for OER catalysis is desired, it is beyond the scope of this study. Consequently, performance trends were determined from the obtained data normalized by multiple methods.

For each normalization method, the overpotentials were compared at relevant current densities. For the geometric surface area, 10 mA cm^{-2} was selected based on reporting conventions in the literature. For all other methods, the appropriate current density was selected such that the region being compared was similar to that for 10 mA cm^{-2} in the geometric surface area assessment, and such that the current was within the Tafel region for the majority of the non-PGMs tested. Additionally, the activity of the Au RDE working electrode was obtained without a catalyst layer to ensure the Au substrate was not significantly contributing to measured activities; these results are included in Fig. S2 of the SI.

IrO_2, the state-of-the-art OER catalyst for PEM electrolyzers, was used as a benchmark in this study (shown in black in Fig. 2). Note that IrO_2 is likely not a feasible candidate for use in commercial AEM systems due to the tendency for Ir to oxidize into soluble forms at high pH and due to its high capital cost;[6] however, as this material is the current standard for PEM electrolysis and is widely used in many device-level AEM publications, it is studiedhere to provide context and establish general performance targets for the non-PGM oxides tested. For the data normalized by the geometric surface area (Fig. 2a), IrO_2 showed the lowest overpotential (<300 mV) at the onset of OER, an exchange current density on the order of 10^{-6} mA/μg_M, and a moderate Tafel slope below 1.55 V (70 mV/dec) which increased to 120 mV/dec at approximately 1.6 V, consistent with results reported in previous studies.[16,40,41] These changes to the Tafel slope can be directly related to changes in kinetic mechanism, specifically in either the identity of the rate determining step or in the surface coverage; in later sections, we discuss the differences in Tafel slope as it relates to possible differences in kinetic mechanism for IrO_2 and non-PGM oxides. Note that above ~1.8 V the Tafel slope continues to increase for IrO_2, (and, in fact, for all samples); while such changes may be indicative of additional changes in kinetic mechanism, this cannot be easily distinguished from changes related to transport limitations of evolved $O_2(g)$ leaving the catalyst surface and, therefore, changes to the Tafel slope above 1.8 V are not considered in discussions of changes in the kinetic mechanism.

The composition of the IrO_2 sample was evaluated via XRD. The diffractograms of this sample (Fig. S3, SI) confirmed the presence of IrO_2 ($2\Theta = 30°$–$40°$, amorphous[42]); however, these diffractograms also indicated that the sample contained large Ir nanoparticles ($2\Theta = 40°$, 47.5°, 69°, and 84°, closely matching JCPDS card 46–1044; crystalline size 20 nm). Ir metal is expected to be more active than IrO_2; previous works have reported 2-times higher site-specific activity for Ir vs IrO_2[16,40,41] and 10-times higher activity per geometric surface area of the electrode for Ir vs IrO_2.[16] Despite the possible inhomogeneity of the as-received IrO_2 sample, and subsequent differences in Ir/IrO_2 ratio loaded on the RDE, the activities of seven replicates were found to be similar (Fig. S4, SI). We hypothesize that the contribution of Ir metal on measured activities was compensated by the larger particle sizes of Ir (and thus lower surface areas) relative to those of IrO_2, resulting in negligible changes in activity with different Ir/IrO_2 ratios. However, the degree of deactivation of four replicates varied significantly; two samples showed an improvement in activity (by 33%–43%) and two samples showed deactivation (by 69%–76%). Ir and IrO_2 have been shown to have different deactivation rates in acidic media due to differences in their dissolution kinetics; Ir has been found to dissolve at a faster rate than IrO_2, which is suggested to be the result of oxidation into soluble forms.[6,41] Oxidation kinetics are expected to increase with increasing pH (higher OH^- concentration), and thus we expect that Ir deactivation via this Ir oxidation and dissolution mechanism would be exacerbated in alkaline media. Therefore, we hypothesize that samples with higher deactivation rates were those with higher Ir metal contents. This is discussed further in the section on stability.

Both Mn_2O_3 and Fe_2O_3 exhibited high overpotentials (>500 mV) across all current density regimes, regardless of the normalization method (shown in magenta and red, respectively, in Fig. 2). Poor OER activity of Mn-based materials has been well-reported in literature; Mn content has been shown to increase the overpotential for OER in ferrous (MFe_2O_4)[43] and cobalt-based spinel ($M_xCo_{3-x}O_4$)[44] materials. Interestingly, Mn_2O_3 had a significantly higher exchange current density than Fe_2O_3 (on the order of 10^{-6} mA/μg_M for Mn_2O_3 vs 10^{-11} mA/μg_M for Fe_2O_3) suggesting that Mn_2O_3 had faster inherent kinetics than Fe_2O_3. However, Mn_2O_3 also exhibited a higher Tafel slope than Fe_2O_3 (120 mV dec^{-1} for Mn_2O_3 vs 60 mV dec^{-1} for Fe_2O_3 for data normalized by the geometric surface area, Fig. 2a). A higher Tafel slope translates to a larger overpotential required to increase the rate by an order of magnitude, and, consequently, high Tafel slopes are often associated with poor performing catalysts. Poor OER activity of Fe_2O_3 has been reported previously and has been attributed to the low electrical conductivity of Fe[45–47] and the non-optimal binding strength of O

Table I. Physical and electrochemical properties of the screened catalysts.

Catalyst material		Supplier	Reported particle size (nm)	BET surface area (m^2/g)	Crystalline Phase	Crystalline size from XRD (nm)	Double layer capacitance (μF)
IrO_2		Alfa Aesar	5	21.1	Amorphous	N/A[a], 19.6[b]	50.0
Mn_2O_3		US Research Nanomaterials	30	30.6	Cubic	21.3	9.4
Fe_2O_3		US Research Nanomaterials	20–40	92.4	Spinel	10.3	57.3
Co_3O_4	A	US Research Nanomaterials	10–30	36.6	Spinel	15.5	10.3
	B	Particular Materials	14	91.0	Spinel	9.6	10.4
NiO		US Research Nanomaterials	10–20	77.2	Cubic	8.7	6.3
$NiFe_2O_4$	A	US Research Nanomaterials	30	76.9	Spinel	10.9	14.2
	B	Nanografi	25	55.2	Spinel	12.9	10.6
	C	Sigma Aldrich	<50	76.9	Spinel	11.1	29.6
$CoNiO_2$		US Research Nanomaterials	20	20.3	Tetragonal	17.6[c], 11.3[d]	11.5

a) IrO_2; broad peak did not allow for d-spacing calculation b) Ir c) Co_3O_4 d) NiO.

intermediates on Fe.[17,48] Burke et al. found in their study of ultra-thin film oxy(hydroxides) that FeO_xH_y had the highest turnover frequency (defined as the number of O_2 molecules evolved per second per metal site), when compared to monometallic (oxy) hydroxides of Mn, Co, and Ni,[24] suggesting that Fe sites can have high activity for OER when the conductivity limitation is mitigated. Furthermore, combing Fe with Ni can lead to better O-binding energetics and improved activity.[48] In fact, Fe sites are often used as dopants in multimetallic OER catalysts such as $NiFe_2O_4$, which will be discussed in detail later.

NiO exhibited much lower overpotentials (~200 mV lower) than Fe_2O_3 and Mn_2O_3 across current density regimes and normalization methods (shown in yellow in Fig. 2). Additionally, NiO performance approached that of IrO_2 above 10 mA cm^{-2} and 1 mA/μg_M when the current densities were normalized by the geometric surface area (Fig. 2a) and metal loading (Fig. 2d), respectively. In fact, NiO showed higher activity than IrO_2 across current density regimes (0.05 to 1 mA μF^{-1}) when the current densities were normalized by the double layer capacitance (Fig. 2c). Furthermore, NiO had an exchange current density on the order or 10^{-6} mA μg_M^{-1}, similar to that of IrO_2. Note that a curved, vertical feature was observed for NiO between $\eta = 200$–300 mV; such a feature was likely caused by NiO oxidation to NiOOH.[49–51] This feature was also present for the other normalization methods but at lower current densities than those plotted in Figs. 2a, 2b, and 2d. Although NiO has been previously reported to exhibit high OER activity,[20–22] this has often been attributed to a trace amount of Fe impurities present either in the electrolyte[23,52] or in the oxide lattice.[23,52,53] To exclude any effects of Fe contamination in the electrolyte, a Pt electrode was held in the electrolyte solution at −0.5 V for 900 s to electrochemically plate out possible contaminants before testing; any Fe ions in solution should reduce and deposit onto the Pt electrode as metal at such potentials. No change in NiO performance before and after the contaminant removal procedure was observed (Fig. S5, SI), indicating that the electrolyte was free of Fe contaminants. It is possible, however, that Fe was present in the as-received NiO sample due to contamination during synthesis.

Co_3O_4 showed the highest activity of all tested non-PGM oxide catalysts, exhibiting the lowest overpotential for OER (~500 mV, Figs. 2e–2h) across normalization methods and across the current density regimes tested (shown in blue in Fig. 2). Additionally, Co_3O_4 surpassed IrO_2 performance at high current densities (>10 mA cm^{-2}) across all normalization methods except by the BET surface area, for which Co_3O_4 instead approached IrO_2 performance (Figs 2b, 2f). This sample had an exchange current density on the order of 10^{-8} mA/μg_M and a Tafel slope of 60 mV dec^{-1}. While Co-containing materials have been reported in the literature to have high OER performance—a result which has been attributed to high electrical conductivity,[54] highly mobile oxygen vacancies,[55,56] and the presence of multiple oxidation states in Co spinel materials[19]—few studies have reported Co_3O_4 performance exceeding that of IrO_2. A Co_3O_4 sample from a different supplier was also evaluated to confirm that Co_3O_4 performance was not sample-specific (Fig. 3). The two samples had the same spinel structure, as confirmed by XRD diffractograms (Fig. S6, SI) and nearly identical double-layer capacitances (approximately 10 μF for each). The samples, however, had different BET surface areas (40 vs 90 m^2 g^{-1} for Co_3O_4 A and B samples, respectively; Table I) due to the difference in their particle sizes (15.5 vs 9.6 nm from XRD for Co_3O_4 A and B samples, respectively; Table I). These samples had nearly identical performance across normalization methods (Fig. 3), except by the BET surface area (Fig. 3b), and both samples surpassed IrO_2 activity at moderate current densities (~5 mA cm^{-2}; Fig. 3a). These results show that although a general correlation is expected between BET and electrochemical surface areas, there are differences in the number of sites that are physically accessible to $N_2(g)$ vs electrochemically accessible to OH^-, posing questions about the relevance of using BET surface area as a normalization method in electrochemical systems. It is also worthwhile to note that the curved feature for Co_3O_4 B is the result of a phase change from Co_3O_4 to CoOOH,[57] which is also present for Co_3O_4 A but at slightly lower current densities.

An assessment of the Tafel slopes for all monometallic oxide materials revealed a possible potential dependence of the mechanism for IrO_2 vs non-PGMs; the Tafel slope for IrO_2 changed at lower current densities (5 mA cm^{-2}_{geo}) than non-PGM oxides (>10 mA cm^{-2}_{geo}). This change is not expected to be related to transport limitations, as the trend persisted when the scan rate was changed (Fig. S7, SI) and no phase change is predicted for this region in Pourbaix diagrams.[6] Moreover, if the deviation was caused by transport limitations of evolved $O_2(g)$, all catalysts should deviate from their linear Tafel regions at the same $O_2(g)$ generation rates, and, therefore, at the same current. Instead, this deviation was more likely the result of a mechanism change, either in the kinetically relevant step or surface coverage of bound intermediates.[8] Conversely, the kinetic region for all non-PGMs extended into the moderate current density regimes; IrO_2 is the only material that exhibited a change in Tafel slope at current densities lower than 10 mA cm^{-2}_{geo}, suggesting that there may be a different kinetic mechanism governing IrO_2 vs non-PGMs. Furthermore, for data normalized by the double-layer capacitance, the change in the Tafel slope for IrO_2 versus non-PGMs was more dramatic. This is in part due to the large double-layer capacitance of IrO_2 obtained from the cyclic voltammetry method (discussed in Section S1, SI); this high double-layer capacitance may be related to the accessibility of "inner" reacting surface sites, as has been suggested for RuO_2.[58] It is also interesting to note slight differences in Tafel slope even among non-PGMs, suggesting that there may be a difference in mechanism (or surface coverages) among these materials. In particular, for current normalized by the geometric surface area, NiO initially had a Tafel slope dissimilar to the other testing Ni-containing materials (120 mV dec^{-1} for NiO vs 60 mV dec^{-1} for other Ni-containing materials) for current densities below 1 mA cm^{-2}, abovewhich all Ni-containing materials had a similar Tafel slope of 120 mV dec^{-1}. This would suggest that Fe and Co dopants change the mechanism on a pure Ni surface, either by changing surface coverage or kinetically relevant steps.

Previous reports have suggested that bimetallic systems, such as Ni-Fe oxides, have higher OER activities than their monometallic counterparts due to the synergy between the two metals.[23–25] $NiFe_2O_4$, however, showed similar overpotentials across all normalization methods (shown in orange and yellow, respectively, in Fig. 2) and similar exchange current densities (on the order of 10^{-6} mA/μg_M for NiO and 10^{-7} mA/μg_M for $NiFe_2O_4$) compared to those of NiO. Such results contradict previous reports that have shown that even a small amount of Fe enhances Ni performance when incorporated into the NiO crystalline structures[23,52,53,59] or in the electrolyte solution.[23,52] Optimal Fe contents proposed by these studies range from 15 to 40 wt% Fe in the bimetallic catalyst,[23,53,59] whereas the $NiFe_2O_4$ spinel material studied in this work contained 66 wt% Fe (by metal content). For NiO, the electrolyte was rigorously cleaned prior to testing (see the section on NiO above and Section S7, SI), ruling out the possibility of Fe contamination in the electrolyte impacting NiO results. Instead, we hypothesize that $NiFe_2O_4$ samples had a prohibitively high Fe content which inhibited its activity. Stability testing of $NiFe_2O_4$ revealed an improvement of performance over time-on-stream concurrent with the increased dissolution of Fe (confirmed from ICP-MS methods), suggesting that an increased Ni/Fe ratio led to the increased performance (discussed in detail in the later section on stability testing).

Figure 4 compares the OER activities of three $NiFe_2O_4$ samples from different commercial suppliers (Table I) and NiO. The OER activities of all $NiFe_2O_4$ samples and NiO were found to be similar across normalization methods; these samples had similar onset potentials (350 to 400 mV) with polarization curves that met at moderate current densities (~1 mA cm^{-2}_{geo}; Fig. 4a). The Tafel behavior of NiO and $NiFe_2O_4$ C closely matched across

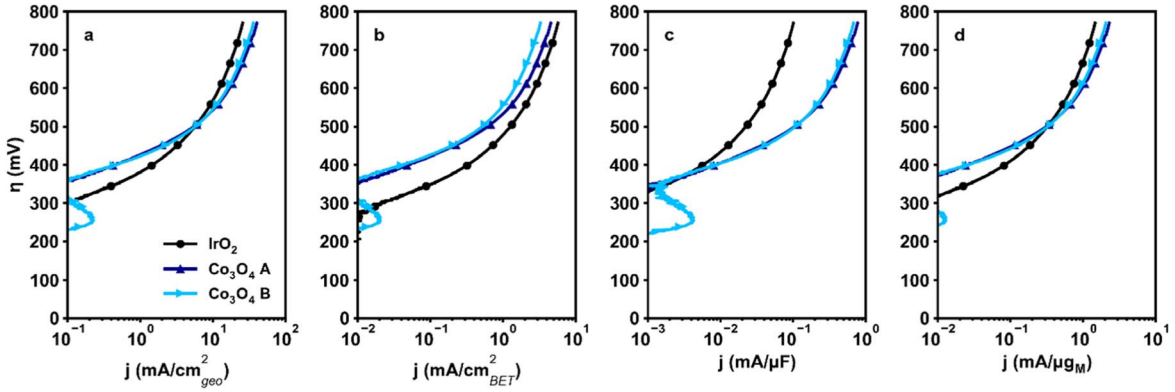

Figure 3. Tafel plots of two Co_3O_4 samples with current densities normalized by (a) geometric surface areas, (b) BET surface areas, (c) double layer capacitances, (d) mass loadings of the metals in oxides. Data were collected at ambient temperature with anRDE rotation rate of 2500 RPM and ascan rate of 20 mV s^{-1}.

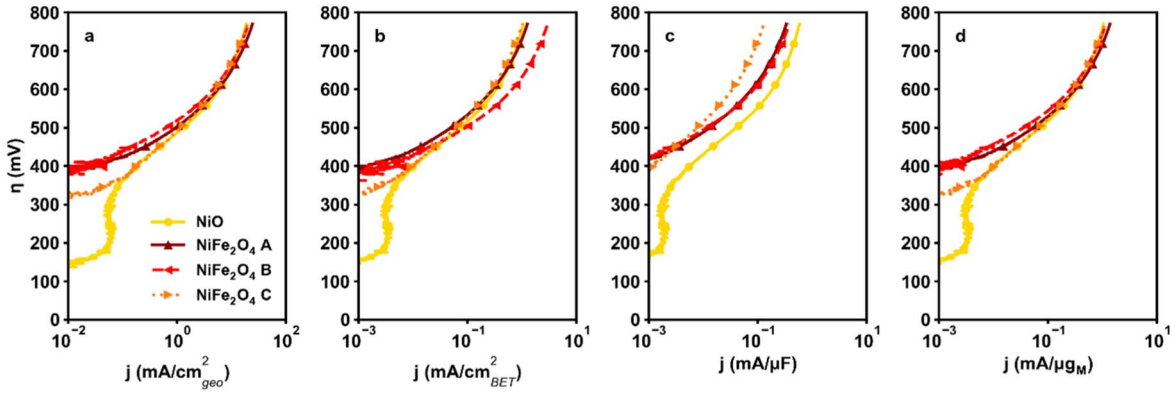

Figure 4. Tafel plots of three $NiFe_2O_4$ samples with activity normalized by the (a) geometric surface area, (b) BET surface area, (c) double layer capacitance, (d) mass loading of metal. Markers are placed at every 25 data points. Data were collected at ambient temperature with an RDE rotation rate of 2500 RPM and a scan rate of 20 mV s^{-1}.

normalization methods (Figs. 4a–4d) and differed slightly from that of $NiFe_2O_4$ A and B; for current normalized by the geometric surface area, NiO and $NiFe_2O_4$ C had Tafel slopes of 120 mV across current densities whereas $NiFe_2O_4$ A and B had Tafel slopes of 60 mV dec^{-1} at overpotentials below ∼500 mV which increased to 120 mV dec^{-1} above $\eta = 500$ mV. Again, Tafel slopes are compared only in the kinetic regime (below ∼1.8 V) to avoid possible interferences from evolved $O_2(g)$ transport in the analysis. To evaluate whether this behavior was caused by structural differences, X-ray diffractograms were obtained for all samples (Fig. 5a). These diffractograms show that all $NiFe_2O_4$ samples contained peaks corresponding to $NiFe_2O_4$ spinel (2Θ = 30.2°, 35.6°, 37.2°, 43.4°, 57.4°, 63.0°, 75.2°, and 80.0°; closely matching JCPDS card 86–2267) with differing amounts of α-Fe_2O_3 contaminants (2Θ = 33.1°, 40.8°, 53.8°, and 64.2°; closely matching JCPDS card 39–1346); these phases are indicated by black dashed and grey dotted lines, respectively, in Fig. 5a. $NiFe_2O_4$ A, $NiFe_2O_4$ B, and $NiFe_2O_4$ C, were composed of 5.0%, 23.1%, and 3.4% of the α-Fe_2O_3 phase, respectively. These values were estimated from the ratio of the area of the most prominent peak assigned to the α-Fe_2O_3 phase (2Θ = 33.1°) vs the sum of this α-Fe_2O_3 peak area and the area of the most prominent peak assigned to the $NiFe_2O_4$ phase (2Θ = 35.6°). The differences in Tafel behavior for materials with different quantities of the α-Fe_2O_3 phase pose questions about the

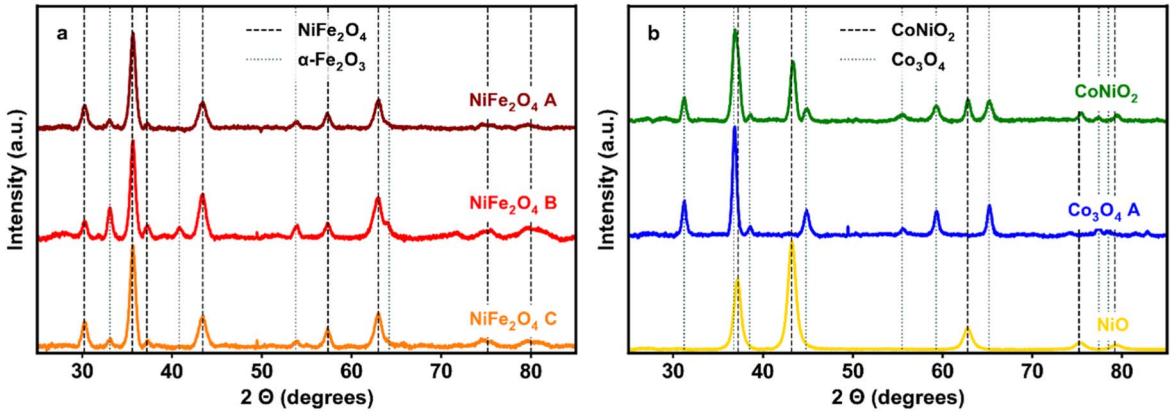

Figure 5. X-ray diffractograms with peaks identified for (a) three $NiFe_2O_4$ samples and (b) $CoNiO_2$, Co_3O_4, and NiO samples.

relative activities and kinetic mechanisms of these different phases of Fe. Furthermore, $NiFe_2O_4$ C, which had the greatest amount of α-Fe_2O_3, showed the largest double-layer capacitance, while $NiFe_2O_4$ A, which had the least amount of α-Fe_2O_3, showed the smallest double-layer capacitance (Figs. 5a, 5b). The α-Fe_2O_3 and $NiFe_2O_4$ phases have different magnetic properties (α-Fe_2O_3 is weakly ferromagnetic at room temperature whereas $NiFe_2O_4$ is ferrimagnetic)[60,61] which have been linked to differences in catalytic activities.[62,63] Differences in physical surface area and crystalline size were also evaluated for all $NiFe_2O_4$ samples to investigate a possible particle size effect. Samples A and C had comparable crystalline sizes and BET surface areas (10 nm and 75 m^2 g^{-1}, respectively), while sample B had a slightly larger crystalline size and thus slightly lower surface area (~13 nm and ~55 m^2 g^{-1}; Table I). These differences, however, did not impact performance; sample B showed similar overpotentials to sample A across current density regimes and normalization methods, excluding by BET surface area (Figs. 4a–4d). This suggests that for the $NiFe_2O_4$ samples evaluated, crystalline size was a less significant factor in determining performance, although the samples tested may not have provided enough range to observe significant effects of particle sizes.

The OER reactivity of $CoNiO_2$ was compared to that of Co_3O_4 and NiO (shown in green, blue, and yellow in Fig. 2, respectively, and separately in Fig. S8 in SI) to assess any possible synergy between Ni and Co. Compared to Co_3O_4, $CoNiO_2$ showed higher overpotentials across current densities and normalization methods (~50 mV larger) and a similar exchange current density (on the order of 10^{-8} mA/μg_M for both $CoNiO_2$ and Co_3O_4). In contrast, when compared to NiO, $CoNiO_2$ had a similar overpotential but a larger exchange current density (10^{-8} mA/μg_M for $CoNiO_2$ and 10^{-6} mA/μg_M for NiO). $CoNiO_2$ had a comparable double-layer capacitance (10.3 vs 11.5 μF for $CoNiO_2$ and Co_3O_4, respectively; Table I) to Co3O4, but a smaller BET surface area (20.3 vs 36.6 m^2 g^{-1} for $CoNiO_2$ and Co_3O_4, respectively; Table I). X-ray diffractograms for $CoNiO_2$ (Fig. 5b) showed peaks matching both $CoNiO_2$ (2Θ = 37.2°, 43.2°, 62.8°, 75.2°, and 79.2°; closely matching JCPDS Card 10–0188) and Co_3O_4 (2Θ = 31.2°, 36.8°, 38.5°, 44.8°, 55.5°, 59.3°, 65.2°, 77.4°, and 78.5°; closely matching JCPDS card 43–1003) with different crystalline sizes (11.3 vs 17.6 nm for $CoNiO_2$ and Co_3O_4, respectively; Table I). These phases are indicated by black dashed and grey dotted lines, respectively, in Fig. 5b. The crystalline size of Co_3O_4 in the mixed oxide was comparable to that of monometallic Co_3O_4 (17.6 vs 15.5 nm for Co_3O_4 in $CoNiO_2$ and Co_3O_4 (monometallic), respectively; Table I), pointing away from a particle size effect being the cause of decreased activity for $CoNiO_2$ vs Co_3O_4. The fact that $CoNiO_2$ had lower activity than Co_3O_4 alone may be due to a difference in the Co oxidation state between these two materials; the Co oxidation state in $CoNiO_2$ is 2+, vs 2.67+ (average) in Co_3O_4 and 3+ in CoOOH. The CoOOH phase is likely formed before OER onset based on the curved feature in Co_3O_4 Tafel plots and reported phase diagrams for Co.[6,57] It is further possible that differences in catalyst synthesis procedures, including the possibility of surfactants left on the surface and blocking sites, may be masking potential Ni-Co synergy advantages.

In summary, our RDE activity screening results suggest that Fe_2O_3 and Mn_2O_3 are less-feasible candidates as OER catalysts. In contrast, Co_3O_4 was found to be the highest-performing catalyst across normalization methods, and NiO and $NiFe_2O_4$ had similar and relatively high OER activities. These RDE results show that non-PGMs, such as Co_3O_4 and Ni-containing materials, are therefore viable OER catalysts for integration into AEM devices based on their high OER activities. Next, we discuss their stability and their performance at the device level to further evaluate their possible replacement of IrO_2 catalysts.

Assessments of catalyst stability based on potentiostatic stress testing.—A selection of materials (IrO_2, Mn_2O_3, Co_3O_4, and $NiFe_2O_4$) was evaluated for stability at operating conditions by comparing the current (i at 1.65 V) before and after stressing at 1.8 V for 13.5 h. A potential of 1.65 V was selected for the activity comparison because it lies in the kinetic region for all four catalysts tested; previous works have used 1.55 V to compare kinetic-region activity for OER catalysts,[41] but the late onset potential of Mn_2O_3 necessitated the use of higher voltage. A combination of ICP-MS analyses and assessment of the change in the active surface area via determination of the double-layer capacitance before and after testing was used to assess possible deactivation/activation mechanisms. While the double-layer capacitance has inherent errors when used to compare materials of different identities, it is considered accurate for evaluations between materials of the same identity.[34]

Four independent tests were performed for the IrO_2 sample; these tests showed high variability among experiments, which led to a large error bar in Fig. 6a. Two runs resulted in a significant loss in activity at 1.65 V (by −69% to −76%), while the other two runs exhibited an increase in activity (by +33% to +43%); the activity changes for each sample are shown in Fig. S9 (SI). Such a dramatic

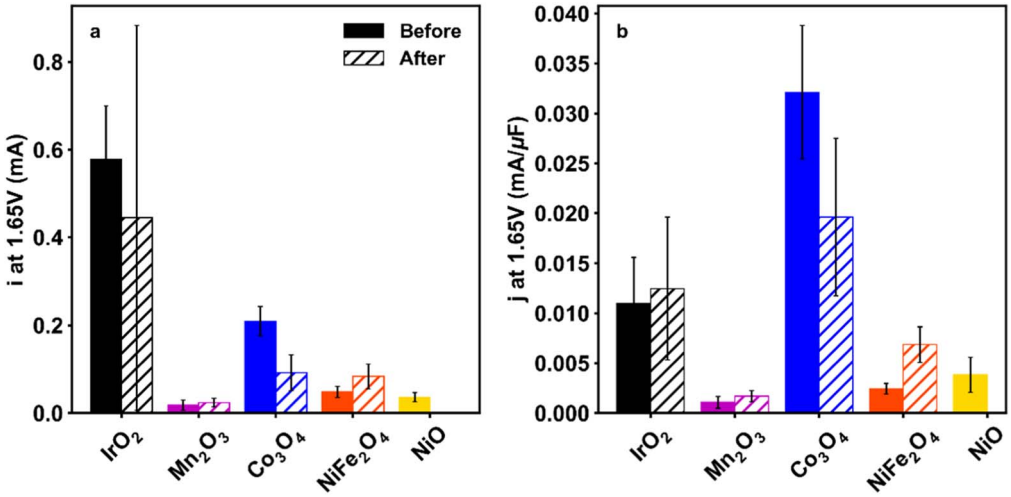

Figure 6. Stability testing results for IrO_2, $NiFe_2O_4$ A, Co_3O_4 A, and Mn_2O_3 represented as the (a) current at 1.65 V and (b) current at 1.65 V normalized by the double layer capacitance before and after the 13.5 h poteniostatic hold at 1.8 V. NiO activity is included for comparison with $NiFe_2O_4$; no stability testing was performed for this sample. The RDE tip was rotated throughout the stress test (2500 RPM). Linear sweep voltammetry data was collected at ambient temperature with an RDE rotation rate of 2500 RPM and a scan rate of 20 mV s^{-1}. Bars and error lines represent the average and standard deviation of at least two runs, respectively.

activity loss was not related to the dissolution of Ir into the solution; ICP-MS analysis of the used electrolyte revealed that all samples showed only a small loss of Ir that was similar among the four runs (1%–4%; Table SVI, SI). Instead, we hypothesize that the discrepancy among replicates is related to the inhomogeneity of the as-received IrO_2 sample. As discussed in the previous section, initial activities for all runs were similar; this is likely attributed to the largercrystalline size (and, relatedly, smaller surface area) of Ir metal compensating for its predicted higher activity,[16,41] thereby resulting in the similar initial activity regardless of Ir metal content. Upon exposure to elevated potential, those large Ir metal nanoparticles would be oxidized into large IrO_2 particles; it is expected that these large IrO_2 particles would be essentially inactive due to the inherently lower activity of IrO_2 vs Ir metal and large particle sizes. Indeed, the errors among four different IrO_2 runs diminished when the results were normalized by the double-layer capacitance determined before and after stability testing (Fig. 6b).

Mn_2O_3 samples did not deactivate within experimental error, and results were consistent between samples both for measured current and for current normalized by the double-layer capacitance. ICP-MS results indicated a mass loss of ∼1% for all Mn samples (Table SVII, SI). The activity of Mn_2O_3 remained lower relative to the other tested samples.

Co_3O_4 samples significantly deactivated over time-on-stream (by 45%–71%; Fig. 6a). Such a deactivation percentage decreased to 29%–54% when the current was normalized by double-layer capacitance measured before and after stressing (Fig. 6b), suggesting that Co_3O_4 deactivation was partially due to a loss in active surface area. A loss in active surface area can be caused by delamination, dissolution, catalyst oxidation, or particle growth. ICP-MS results indicated minimal Co dissolution (mass loss: <0.1%; Table SVIII, SI), and Co delamination losses are expected to be minimized by the RDE coating technique utilized.[35,41] Furthermore, if Co delamination had occurred, the activity drop would be expected to be larger; therefore, Co loss (dissolution or delamination) was not responsible for deactivation. Instead, we hypothesize that the mechanism of catalyst deactivation was caused by oxide growth and, relatedly, particle growth, which led to a decrease in active surface area; this is supported by an observed decrease in the double-layer capacitance (∼30%) for the Co_3O_4 samples (Fig. S10, SI). Additional catalyst deactivation may have been caused by decreased electrical conductivity with increasing oxide content. At the device level, the implications of Co_3O_4 deactivation via oxide and particle growth would require the development of conditioning procedures that could minimize and stabilize this deactivation method.

The activity of $NiFe_2O_4$ increased after stress testing (+60% to +87%; shown in orange, Fig. 6). As discussed above, the synergy between Ni and Fe for OER is well-discussed in literature, where bimetallic systems of these two metals have often shown higher activity compared to their monometallic counterparts.[23,52,53] Initial activities of the three $NiFe_2O_4$ samples evaluated in this study, however, matched the activity of NiO (Fig. 4), possibly because the as-received $NiFe_2O_4$ samples had too-high Fe content (66 wt% Fe by metals content); the most active compositions reported in literature ranged between 15 to 40 wt% Fe.[23,53] We hypothesize that the observed activity increase of $NiFe_2O_4$ after stability testing was due to Fe dissolution and a decrease in Fe content. In fact, ICP-MS results showed that the three tested samples had mass losses between 2 to 8% (Table SIX, SI), where increased Fe dissolution correlated to increased activity. Additionally, the extent of improvement increased from 60%–87% to 147%–203% when the current was normalized by the double-layer capacitance. Normalization by the double-layer capacitance was performed to capture changes in the active surface area upon stressing; the double-layer capacitance for these samples decreased by 24%–47%. These results seem to suggest that the improvement, at least in part, was due to a change

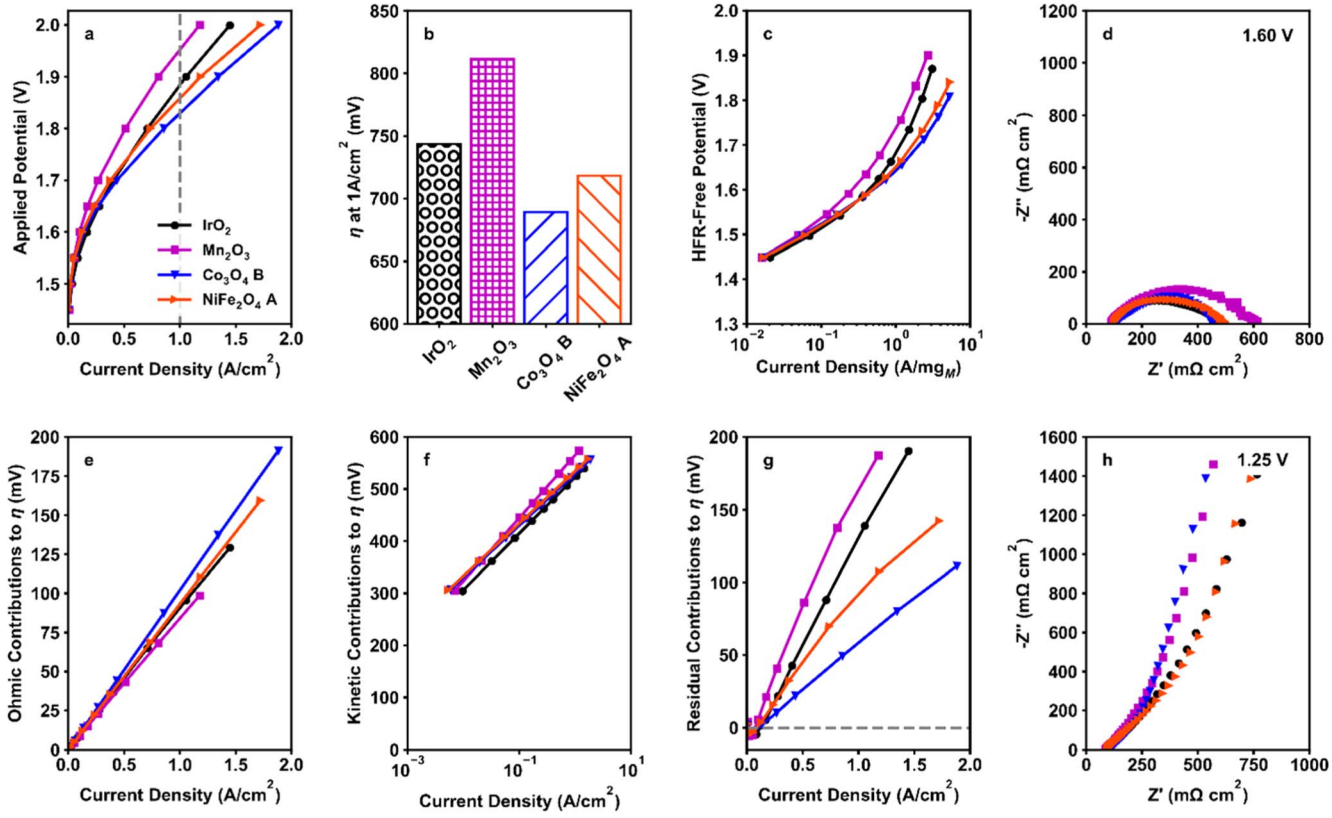

Figure 7. MEA results for IrO_2, Mn_2O_3, Co_3O_4 B, and $NiFe_2O_4$ A. (a) polarization curves, (b) bar plots of the overpotential a 1 A cm^{-2} (c) Tafel plots of the HFR-free potential vs the current normalized by the mass loading of metals, (d) EIS at 1.60 V, (e) ohmic contributions to overpotential, (f) kinetic contributions to overpotential, (g) residual contributions to overpotential, (h) EIS at 1.25 V. Data collected at 80 °C. Flow configuration: cathode dry, 50 ml min^{-1} to the anode.

in per-site activity as optimal Fe content was approached. We also note that the improvement in activity for $NiFe_2O_4$ may be related to the development of NiFeOOH surface phases, as NiFeOOH has been shown in the literature to have high activity for OER.[24] No notable changes in redox features were observed in the cyclic voltammograms of this sample before and after testing, suggesting either that there was no phase change, or that such a phase change from $NiFe_2O_4$ to NiFeOOH was immediate upon contact with either air or the NaOH electrolyte. When considering scale-up to the device level, methods to stabilize Fe content at an optimal value while preventing further Fe dissolution are necessary. Specifically, further elucidation of the extent of Fe dissolution over time, the effect of more aggressive stress testing (i.e., cycling), and methods of stabilizing NiFe oxide catalysts with optimal Fe content will be needed to facilitate the scale-up of this material to the device level. Further exploration of the activation of $NiFe_2O_4$ and its possible integration at the device level is the subject of our current work, which will be published at a later time.

Assessments of device-level performance based on MEA testing.—Figure 7 shows the MEA results for IrO_2, Mn_2O_3, Co_3O_4, and $NiFe_2O_4$. While RDE testing provides fundamental insights into thekinetics of thesematerials, MEA testing is required to assess the integration feasibility of these materials at the device level; this method addresses the effects of incorporating the catalyst layer with the anion exchange membrane and gas diffusion and porous transport layers. In fact, RDE and MEA results may vary due to the complex interplay between catalyst, ionomer, and electrolyte, or the effects of device hardware.[40,64–66] Thus, a parallel assessment of RDE and MEA testing is needed to show how integration variables—including ink rheology, catalyst-ionomer interaction, and catalyst layer structure and uniformity—influence the catalytic performance of PGM and non-PGM oxides.

Mn_2O_3 exhibited the highest overpotential across current density regimes, followed by $IrO_2 > NiFe_2O_4 > Co_3O_4$ (Fig. 7a). At 1 A cm^{-2}, Co_3O_4 and $NiFe_2O_4$ both achieved lower overpotentials than IrO_2 (η = 744 mV, 689 mV, and 718 mV for IrO_2, Co_3O_4, and $NiFe_2O_4$, respectively; Fig. 7b), with the overpotential gap increasing with increasing current density (at 1.5 A cm^{-2}, η = 858 mV, 778 mV, 807 mV or IrO_2, Co_3O_4, and $NiFe_2O_4$, respectively). This high activity of $NiFe_2O_4$ at the device level was confirmed to be consistent across multiple experiments; three independent replicates showed similar performance across current density regimes (Fig. S11, SI).

Figure 7c shows the HFR-free potential as a function of mass-specific current; trends between materials obtained in the Tafel region (here, up to about 1.6 V) of HFR-free potentials (Fig. 7c) are assumed to be related, primarily, to kinetic differences, and, therefore, these results can be reasonably compared to RDE results. HFR is related to ohmic losses from the membrane and cell hardware, contact resistances, and bulk resistances of the diffusion media, and can be calculated from electrochemical impedance spectroscopy (EIS) measurements at each potential of the polarization curve (this method is discussed in detail in Section S16 of the SI). In Fig. 7c, IrO_2, $NiFe_2O_4$, and Co_3O_4 all had similar activity for OER up to 1.6 V, which was consistent with the EIS results (1.60 V; Fig. 7d), which indicated that these materials have similar charge transfer resistances (related to the diameter of the hemispherical curve). The polarization results from this region (Fig. 7c) loosely followed trends from RDE testing, where Mn_2O_3 had the highest overpotential of all tested materials, Co_3O_4 had a similar overpotential to IrO_2 at 10 mA cm^{-2}_{geo} (500 mV), and $NiFe_2O_4$ had a slightly higher overpotential than Co_3O_4 and IrO_2 across current density regimes. Additionally, as in RDE testing, IrO_2 deviated from Tafel kinetics at lower current densities than non-PGM materials in MEA testing; this may again be indicative of differences in mechanism for IrO_2 vs non-PGM materials. Slight differences in kinetic activity trends (i.e., in RDE there was a separation between activity for IrO_2, Co_3O_4, and $NiFe_2O_4$ whereas in MEA testing these materials had similar activity in the Tafel region, Fig. 7c) likely resulted from differences in catalyst layer microstructure and properties (resistances, ionomer distribution, and interfacial contacts) which are not applicable at the RDE level. Furthermore, differences observed between materials at current densities beyond those associated with Tafel kinetics (potentials > 1.6 V, Figs. 7a and 7c) were likely influenced by device integration parameters (i.e., between anode and cathode catalyst layers and the anion exchange membrane andporous transport layers) and emphasize the importance of testing at the RDE and MEA levels in parallel at the catalyst screening and development stages.

Measured overpotentials were separated into ohmic, kinetic, and residual contributions via a voltage breakdown analysis (Figs. 7e–7g; analysis details in Section S16 of the SI). Among all catalysts, the ohmic contributions to overpotential were similar (see Fig. 7e), matching expectations as all materials were tested using the same membranes and cell hardware. Kinetic contributions to overpotential (Fig. 7f) were also similar between samples, with Tafel slopes found to be between 90 and 100 mV dec^{-1}. The most significant differences in performance, however, were found to be attributable to the residual contributions to overpotential (Fig. 7g); this factor is expected to be inclusive of the transport of the KOH electrolyte through the catalyst layer, transport of $O_2(g)$ products away from the catalyst layer, and of catalyst layer resistances (including catalyst-ionomer interactions).

A combination of EIS analysis, loading-change experiments, and conditioning time experiments was utilized to probe the origin of residual contributions to overpotential in MEA testing. Anode catalyst loading was changed to assess possible differences in site accessibility related to the thickness of the catalyst layer. For Co_3O_4, minimal performance differences were found between loadings for Co_3O_4 B (0.2 to 0.6 mg cm^{-2}), suggesting that all sites were fully accessible for this material in the catalyst loading ranges tested (Fig. S12, SI). Note that there may be additional trends observed at higher loading intervals; however, this is outside the scope of this publication. For $NiFe_2O_4$, thicker catalyst layers (2.0 mg cm^{-2} vs 0.5 mg cm^{-2}) resulted in higher ohmic losses and lower activity (Fig. S13, SI). Changes to catalyst conditioning time for Co_3O_4 B and IrO_2 were performed to assess differences in catalyst layer stabilization (Figs. S14 and S15, SI), and minimal differences were found between conditioning results for samples with different catalyst loadings; all samples exhibited a stabilization of performance at 30 ks in a test lasting 100 ks. For assessments of conditioning time for IrO_2, stabilization of performance was similarly achieved at 30 ks up to the tested duration of 100 ks.

EIS in the non-Faradaic region (1.25 V; Fig. 7h) was obtained to study catalyst layer resistances and their role in residual contributions to overpotential. The study of catalyst layer resistances and their features in EIS has been discussed for electrochemical devices generally;[67–70] in short, catalyst layer resistances are inclusive of electronic and ionic resistances in the catalyst layer, which, in turn, consists of the catalyst (electron-conducting phase) and ionomer (ion conducting phase). High catalyst layer resistances can lead to an uneven distribution of overpotential, poor catalyst utilization, and high voltage losses as current density increases; therefore, an understanding of catalyst layer resistances is key to minimizing overpotential losses. In this work, catalyst layer resistances were found using transmission line theory for porous electrodes,[67] where the catalyst layer resistance was assumed to be equal to three times the width of the 45° region at high-frequencies in non-Faradaic EIS. This method is discussed in Section S20, SI. The results show that catalyst layer resistances increased with $Co_3O_4 < Mn_2O_3 < NiFe_2O_4 < IrO_2$ (Table SX, SI). These resistances, in part, account for the differences in residual contributions to overpotential and the deviation of Tafel slopes at moderate current density (Fig. 7c). More importantly, these results provide an avenue for further optimization of AEM device-level performance; catalyst layer resistances can be decreased through novel PTL design and through optimization of catalyst layer architecture such as catalyst layer thickness, the ratio

of catalyst/ionomer, and catalyst-ionomer integration. While a full analysis and discussion of catalyst layer resistances in AEM systems and their features in EIS is beyond the scope of this study, this is a topic of our future work to be published at a later time.

Thus far, we have discussed the catalytic activity, stability, and device-level integrability of non-PGM catalysts for OER in AEM systems. When determining the scale-up viabilityof OER catalysts, material criticality is also an important consideration, specifically asconcerns over material availability grow for technologies essential to a clean energy transition, including Li-ion batteries[71] and electrolyzers.[5] While a range of methods have been used for determining material criticality, all methods generally include a metric of the supply risk of the material (based on the likelihood of supply disruption, ranging from projected material costs, the political or economic stability of countries of origin, and recyclability of material) and of the vulnerability of a system (i.e. the global economy, a given country, a company, or a given technology) to that supply disruption.[72,73] These two metrics are compared and a threshold is established based on the context of the study being performed. Several recent works have evaluated materials relevant to electrolyzers using such methods; for example, in a recent review by Schrijvers et al.[72] which considered criticality assessments across a variety of methods from a variety of stakeholders, it was found that in all reviewed criticality assessments, Co had "high" material criticality more than 2-times as often as Ni or Fe.[72] Furthermore, Co is currently a key component in Li-ion batteries and has appeared on critical materials lists alongside PGMs such as Ir globally.[5,28,31] Such a high criticality of Co, in turn, poses questions about the validity of its use as IrO_2 replacement, despite its high initial OER reactivity as shown in this work.

Conclusions

This work evaluated non-PGM nanoparticles in their oxide forms to assess their use as the OER catalyst in AEM electrolyzers. Among the commercial non-PGM catalysts tested, Co_3O_4 and Ni-containing compounds, including NiO and $NiFe_2O_4$, showed high activity in both RDE and MEA testing. In RDE testing, these trends persisted for current normalized by the geometric surface area of the electrode, the double-layer capacitance, and the mass loading of metals. In terms of catalyst stability, Co_3O_4 deactivated over time-on-stream (13.5 h, RDE testing) via particle oxidation and growth; device-level comparisons involving this material should therefore be made after suitable conditioning procedures (i.e., after the surface has been allowed to fully oxidize). In contrast, $NiFe_2O_4$ increased in activity over time-on-stream due to the dissolution of Fe and an increased Ni/Fe ratio. At the device level, non-PGMs Co_3O_4 and $NiFe_2O_4$ had similar overpotentials to IrO_2 in the kinetic regime and lower overpotentials than IrO_2 for current densities > 1 A cm^{-2}. We also observed that for high current density regimes (>0.5 A cm^{-2}), catalyst activity trends wereclosely related to trends in residual contributions to overpotential, including catalyst layer resistances. These results provide new perspectives into the possibility of using $NiFe_2O_4$ as an IrO_2-replacement catalyst for OER in AEM electrolyzers, as well as offer guidance as to important considerations in scaling from RDE testing to the device level.

This work highlights the broad and critical need for (1) the development of methods to determine the real electrochemical surface area of non-PGM oxides in-situ and, in turn, advance fundamental understanding of electrocatalytic activities and mechanisms, (2) further assessment of the differences in the Tafel behavior observed for IrO_2 vs non-PGMs, (3) understanding of relevant $NiFe_2O_4$ phases in-situ and how this relates to optimal Fe content, with an emphasis on how to stabilize catalysts at such a Fe content, and (4) optimization of catalyst layer properties to facilitate minimization of catalyst layer resistances. Furthermore, this work emphasizes the importance of conducting ex-situ (RDE) and in-situ (MEA) testing in parallel to simultaneously gain insights into fundamental catalyst activity as well as catalyst layer structure/composition and device integration. Lastly, considerations of material cost, criticality, and scalability must be made when considering materials to serve as PGM replacements in AEM electrolyzers.

Acknowledgments

We thank Dr. Saad Intikhab (NREL) for training in MEA assembly and operation; Dr. Elliot Padgett (NREL) for training in EIS; Yingxue Bian (Mines) for training in N_2 physisorption; and Kemakorn Ithisuphalap (Mines), Jesse Dugan (Mines), and Melissa Kreider (NREL) for providing careful proofreading of this manuscript. We acknowledge financial support from the HydroGEN 2.0 LTE consortium. SK acknowledges startup funding from Colorado School of Mines. This work was authored by the National Renewable Energy Laboratory, operated by Alliance for Sustainable Energy, LLC, for the U.S. Department of Energy (DOE) under Contract No. DE-AC36–08GO28308. The views expressed in the article do not necessarily represent the views of the DOE or the U.S. Government. The U.S. Government retains, and the publisher, by accepting the article for publication, acknowledges, that the U.S. Government retains a nonexclusive, paid-up, irrevocable, worldwide license to publish or reproduce the published form of this work or allow others to do so, for U.S. Government purposes.

ORCID

Emily K. Volk https://orcid.org/0000-0002-8828-329X
Stephanie Kwon https://orcid.org/0000-0001-7759-0481
Shaun M. Alia https://orcid.org/0000-0002-7647-9383

References

1. B. Pivovar, N. Rustagi, and S. Satyapal, "Hydrogen at scale (H2@Scale): key to a clean, economic, and sustainable energy system." *Electrochem. Soc. Interface*, **27**, 47 (2018).
2. R. Borup, T. Krause, and J. Brouwer, "Hydrogen is essential for industry and transportation decarbonization." *Electrochem. Soc. Interface*, **30**, 79 (2021).
3. IRENA, Green Hydrogen Cost Reduction - Scaling up Electrolyzers to Meet the 1.5C Climate Goal; International Renewable Energy Agency. https://irena.org/publications/2020/Dec/Green-hydrogen-cost-reduction (2020), (accessed 2022-08-18).
4. S. Alia, D. Ding, A. McDaniel, F. M. Toma, and H. N. Dinh, "Chalkboard 2 - how to make clean hydrogen." *Electrochem. Soc. Interface*, **30**, 49 (2021).
5. S. Kiemel, T. Smolinka, F. Lehner, J. Full, A. Sauer, and R. Miehe, "Critical materials for water electrolysers at the example of the energy transition in Germany." *Int. J. Energy Res.*, **45**, 9914 (2021).
6. M. Pourbaix, "Atlas of electrochemical equilibria in aqueous solutions." *NACE*, **13**, 471 (1974).
7. H. A. Miller, K. Bouzek, J. Hnat, S. Loos, C. I. Bernäcker, T. Weißgärber, L. Röntzsch, and J. Meier-Haack, "Green hydrogen from anion exchange membrane water electrolysis: a review of recent developments in critical materials and operating conditions." *Sustain. Energy Fuels*, **4**, 2114 (2020).
8. J. Parrondo, C. G. Arges, M. Niedzwiecki, E. B. Anderson, K. E. Ayers, and V. Ramani, "Degradation of anion exchange membranes used for hydrogen production by ultrapure water electrolysis." *RSC Adv.*, **4**, 9875 (2014).
9. C. G. Arges, V. K. Ramani, and P. N. Pintauro, "The chalkboard: anion exchange membrane fuel cells." *Electrochem. Soc. Interface*, **19**, 31 (2010).
10. D. Li, I. Matanovic, A. S. Lee, E. J. Park, C. Fujimoto, H. T. Chung, and Y. S. Kim, "Phenyl oxidation impacts the durability of alkaline membrane water electrolyzer." *ACS Appl. Mater. Interfaces*, **11**, 9696 (2019).
11. G. A. Lindquist, S. Z. Oener, R. Krivina, A. R. Motz, A. Keane, C. Capuano, K. E. Ayers, and S. W. Boettcher, "Performance and durability of pure-water-fed anion exchange membrane electrolyzers using baseline materials and operation." *ACS Appl. Mater. Interfaces*, **13**, 51917 (2021).
12. S. Ghoshal, B. S. Pivovar, and S. M. Alia, "Evaluating the effect of membrane-ionomer combinations and supporting electrolytes on the performance of cobalt nanoparticle anodes in anion exchange membrane electrolyzers." *J. Power Sources*, **488**, 229433 (2021).
13. P. Fortin, T. Khoza, X. Cao, S. Y. Martinsen, A. Oyarce Barnett, and S. Holdcroft, "High-performance alkaline water electrolysis using aemion™ anion exchange membranes." *J. Power Sources*, **451**, 227814 (2020).
14. S. Noh, J. Y. Jeon, S. Adhikari, Y. S. Kim, and C. Bae, "Molecular engineering of hydroxide conducting polymers for anion exchange membranes in electrochemical energy conversion technology." *Acc. Chem. Res.*, **52**, 2745 (2019).
15. C. C. L. McCrory, S. Jung, I. M. Ferrer, S. M. Chatman, J. C. Peters, and T. F. Jaramillo, "Benchmarking hydrogen evolving reaction and oxygen evolving reaction electrocatalysts for solar water splitting devices." *J. Am. Chem. Soc.*, **137**, 4347 (2015).
16. G. C. Anderson, B. S. Pivovar, and S. M. Alia, "Establishing performance baselines for the oxygen evolution reaction in alkaline electrolytes." *J. Electrochem. Soc.*, **167**, 044503 (2020).

17. I. C. Man, H.-Y. Su, F. Calle-Vallejo, H. A. Hansen, J. I. Martínez, N. G. Inoglu, J. Kitchin, T. F. Jaramillo, J. K. Nørskov, and J. Rossmeisl, "Universality in oxygen evolution electrocatalysis on oxide surfaces." *Chem. Cat. Chem*, **3**, 1159 (2011).
18. J. T. Mefford, A. R. Akbashev, L. Zhang, and W. C. Chueh, "Electrochemical reactivity of faceted β-$Co(OH)_2$ single crystal platelet particles in alkaline electrolytes." *J. Phys. Chem. C*, **123**, 18783 (2019).
19. H.-Y. Wang, S.-F. Hung, H.-Y. Chen, T.-S. Chan, H. M. Chen, and B. Liu, "In operando identification of geometrical-site-dependent water oxidation activity of spinel Co_3O_4." *J. Am. Chem. Soc.*, **138**, 36 (2016).
20. M. E. G. Lyons and M. P. Brandon, "A comparative study of the oxygen evolution reaction on oxidised nickel, cobalt and iron electrodes in base." *J. Electroanal. Chem.*, **641**, 119 (2010).
21. F. Calle-Vallejo, O. A. Diaz-Morales, M. J. Kolb, and M. T. M. Koper, "Why Is Bulk Thermochemistry a Good Descriptor for the Electrocatalytic Activity of Transition Metal Oxides?" *ACS Catalysis*, **5**, 869 (2015).
22. R. Subbaraman, D. Tripkovic, K.-C. Chang, D. Strmcnik, A. P. Paulikas, P. Hirunsit, M. Chan, J. Greeley, V. Stamenkovic, and N. M. Markovic, "Trends in activity for the water electrolyser reactions on 3d M(Ni,Co,Fe,Mn) hydr(Oxy) oxide catalysts." *Nat. Mater.*, **11**, 550 (2012).
23. L. Trotochaud, S. L. Young, J. K. Ranney, and S. W. Boettcher, "Nickel–Iron oxyhydroxide oxygen-evolution electrocatalysts: the role of intentional and incidental iron incorporation." *J. Am. Chem. Soc.*, **136**, 6744 (2014).
24. M. S. Burke, L. J. Enman, A. S. Batchellor, S. Zou, and S. W. Boettcher, "Oxygen evolution reaction electrocatalysis on transition metal oxides and (oxy)hydroxides: activity trends and design principles." *Chem. Mater.*, **27**, 7549 (2015).
25. L. Trotochaud, J. K. Ranney, K. N. Williams, and S. W. Boettcher, "Solution-cast metal oxide thin film electrocatalysts for oxygen evolution." *J. Am. Chem. Soc.*, **134**, 17253 (2012).
26. Y. Lee, J. Suntivich, K. J. May, E. E. Perry, and Y. Shao-Horn, "Synthesis and activities of rutile IrO_2 and RuO_2 nanoparticles for oxygen evolution in acid and alkaline solutions." *J. Phys. Chem. Lett.*, **3**, 399 (2012).
27. N.-T. Suen, S.-F. Hung, Q. Quan, N. Zhang, Y.-J. Xu, and H. M. Chen, "Electrocatalysis for the oxygen evolution reaction: recent development and future perspectives." *Chem. Soc. Rev.*, **46**, 337 (2017).
28. S. BobbaEuropean Comission; Directorate-General for Internal Market, I. et al., *Report on Critical Raw Materials and the Circular Economy* (Publications Office of the European Union: LU) (2018).
29. T. E. Graedel, B. K. Reck, and A. Miatto, "Alloy information helps prioritize material criticality lists." *Nat. Commun.*, **13**, 150 (2022).
30. A. Charpentier Poncelet, C. Helbig, P. Loubet, A. Beylot, S. Muller, J. Villeneuve, B. Laratte, A. Thorenz, A. Tuma, and G. Sonnemann, "Losses and lifetimes of metals in the economy." *Nat. Sustain.*, **5**, 717 (2022).
31. S. M. Fortier, N. T. Nassar, G. W. Lederer, J. Brainard, J. Gambogi, and E. A. McCullough, *Draft Critical Mineral List—Summary of Methodology and Background Information—U.S. Geological Survey Technical Input Document in Response to Secretarial Order No. 3359*, Open-File Report 2018–1021 U.S. Geological Survey (2018) p. 15.
32. K. M. Krishnan, "7. X-Ray Diffraction." *In Principles of Materials Characterization and Metrology* (Oxford University Press, Oxford) (2021).
33. S. Brunauer, P. H. Emmett, and E. Teller, "Adsorption of gases in multimolecular layers." *J. Am. Chem. Soc.*, **60**, 309 (1938).
34. S. Trasatti and O. A. Petrii, "Real surface area measurements in electrochemistry." *J. Electroanal. Chem.*, **327**, 353 (1992).
35. K. Shinozaki, J. W. Zack, R. M. Richards, B. S. Pivovar, and S. S. Kocha, "Oxygen reduction reaction measurements on platinum electrocatalysts utilizing rotating disk electrode technique: I. Impact of impurities, measurement protocols and applied corrections." *J. Electrochem. Soc.*, **162**, F1144 (2015).
36. M. A. Bird, S. E. Goodwin, and D. A. Walsh, "Best practice for evaluating electrocatalysts for hydrogen economy." *ACS Appl. Mater. Interfaces*, **12**, 20500 (2020).
37. H. A. El-Sayed, A. Weiß, L. F. Olbrich, G. P. Putro, and H. A. Gasteiger, "OER catalyst stability investigation using RDE technique: a stability measure or an artifact." *J. Electrochem. Soc.*, **166**, F458 (2019).
38. A. J. Bard and L. R. Faulkner, *Electrochemical Methods: Fundamentals and Applications* (Wiley, New York) 2nd ed. (2000).
39. T. F. Fuller and J. N. Harb, *Electrochemical Engineering* (Wiley, New York) (2018).
40. S. M. Alia, M.-A. Ha, G. C. Anderson, C. Ngo, S. Pylypenko, and R. E. Larsen, "The roles of oxide growth and sub-surface facets in oxygen evolution activity of iridium and its impact on electrolysis." *J. Electrochem. Soc.*, **166**, F1243 (2019).
41. S. M. Alia, B. Rasimick, C. Ngo, K. C. Neyerlin, S. S. Kocha, S. Pylypenko, H. Xu, and B. S. Pivovar, "Activity and durability of iridium nanoparticles in the oxygen evolution reaction." *J. Electrochem. Soc.*, **163**, F3105 (2016).
42. C. Felix, T. Maiyalagan, S. Pasupathi, B. Bladergroen, and V. Linkov, "Synthesis and optimisation of IrO_2 electrocatalysts by adams fusion method for solid polymer electrolyte electrolysers." *Micro Nanosyst.*, **4**, 186 (2012).
43. M. Li, Y. Xiong, X. Liu, X. Bo, Y. Zhang, C. Han, and L. Guo, "Facile synthesis of electrospun MFe_2O_4 (M = Co, Ni, Cu, Mn) spinel nanofibers with excellent electrocatalytic properties for oxygen evolution and hydrogen peroxide reduction." *Nanoscale*, **7**, 8920 (2015).
44. S. Hirai, S. Yagi, A. Seno, M. Fujioka, T. Ohno, and T. Matsuda, "Enhancement of the oxygen evolution reaction in Mn3+-based electrocatalysts: correlation between jahn–teller distortion and catalytic activity." *RSC Adv.*, **6**, 2019 (2015).
45. M. S. Burke, M. G. Kast, L. Trotochaud, A. M. Smith, and S. W. Boettcher, "Cobalt–Iron (Oxy)hydroxide oxygen evolution electrocatalysts: the role of structure and composition on activity, stability, and mechanism." *J. Am. Chem. Soc.*, **137**, 3638 (2015).
46. D. Friebel et al., "Identification of highly active Fe sites in (Ni,Fe)OOH for electrocatalytic water splitting." *J. Am. Chem. Soc.*, **137**, 1305 (2015).
47. S. Zou, M. S. Burke, M. G. Kast, J. Fan, N. Danilovic, and S. W. Boettcher, "Fe (Oxy)hydroxide oxygen evolution reaction electrocatalysis: intrinsic activity and the roles of electrical conductivity, substrate, and dissolution." *Chem. Mater.*, **27**, 8011 (2015).
48. K. R. Park, J. Jeon, H. Choi, J. Lee, D.-H. Lim, N. Oh, H. Han, C. Ahn, B. Kim, and S. Mhin, "NiFe layered double hydroxide electrocatalysts for an efficient oxygen evolution reaction." *ACS Appl. Energy Mater.*, **5**, 8592 (2022).
49. L.-F. Huang, M. J. Hutchison, R. J. Santucci, J. R. Scully, and J. M. Rondinelli, "Improved electrochemical phase diagrams from theory and experiment: the Ni–water system and its complex compounds." *J. Phys. Chem. C*, **121**, 9782 (2017).
50. Y. Zhou and N. López, "The role of Fe species on NiOOH in oxygen evolution reactions." *ACS Catal.*, **10**, 6254 (2020).
51. B. Yang, C. Shi, J. Teng, X. Gong, X. Ye, Y. Li, Q. Lei, and Y. Nie, "Corrosion behaviours of low Mo Ni-(Co)-Cr-Mo alloys with various contents of Co in HF Acid solution." *J. Alloys Compd.*, **791**, 215 (2019).
52. D. A. Corrigan, "The catalysis of the oxygen evolution reaction by iron impurities in thin film nickel oxide electrodes." *J. Electrochem. Soc.*, **134**, 377 (1987).
53. M. W. Louie and A. T. Bell, "An investigation of thin-film Ni–Fe oxide catalysts for the electrochemical evolution of oxygen." *J. Am. Chem. Soc.*, **135**, 12329 (2013).
54. R. A. Krivina et al., "Anode catalysts in anion-exchange-membrane electrolysis without supporting electrolyte: conductivity, dynamics, and ionomer degradation." *Adv. Mater.*, 2203033 (2022).
55. D. Jiang and S. Dai, "The role of low-coordinate oxygen on Co_3O_4(110) in catalyticco oxidation." *Phys. Chem. Chem. Phys.*, **13**, 978 (2010).
56. L. Xu, Q. Jiang, Z. Xiao, X. Li, J. Huo, S. Wang, and L. Dai, "Plasma-engraved Co_3O_4 nanosheets with oxygen vacancies and high surface area for the oxygen evolution reaction." *Angew. Chem.*, **55**, 5277 (2016).
57. J. T. Mefford, Z. Zhao, M. Bajdich, and W. C. Chueh, "Interpreting tafel behavior of consecutive electrochemical reactions through combined thermodynamic and steady state microkinetic approaches." *Energy Environ. Sci.*, **13**, 622 (2020).
58. S. Ardizzone, G. Fregonara, and S. Trasatti, ""Inner" and "outer" active surface of RuO_2 electrodes." *Electrochim. Acta*, **35**, 263 (1990).
59. M. Görlin, P. Chernev, J. Ferreira de Araújo, T. Reier, S. Dresp, B. Paul, R. Krähnert, H. Dau, and P. Strasser, "Oxygen evolution reaction dynamics, faradaic charge efficiency, and the active metal redox states of Ni–Fe oxide water splitting electrocatalysts." *J. Am. Chem. Soc.*, **138**, 5603 (2016).
60. M. I. Dar and S. A. Shivashankar, "Single crystalline magnetite, maghemite, and hematite nanoparticles with rich coercivity." *RSC Adv.*, **4**, 4105 (2013).
61. L. Sun, R. Zhang, Z. Wang, L. Ju, E. Cao, and Y. Zhang, "Structural, dielectric and magnetic properties of $NiFe_2O_4$ prepared via sol–gel auto-combustion method." *J. Magn. Magn. Mater.*, **421**, 65 (2017).
62. M. A. Oliver-Tolentino, J. Vázquez-Samperio, A. Manzo-Robledo, R. González-Huerta, G. de, J. L. Flores-Moreno, D. Ramírez-Rosales, and A. Guzmán-Vargas, "An Approach to understanding the electrocatalytic activity enhancement by superexchange interaction toward OER in alkaline media of Ni–Fe LDH." *J. Phys. Chem. C*, **118**, 22432 (2014).
63. X. Li, Z. Cheng, and X. Wang, "Understanding the mechanism of the oxygen evolution reaction with consideration of spin." *Electrochem. Energy Rev.*, **4**, 136 (2021).
64. S. A. Mauger, K. C. Neyerlin, S. M. Alia, C. Ngo, S. K. Babu, K. E. Hurst, S. Pylypenko, S. Litster, and B. S. Pivovar, "Fuel cell performance implications of membrane electrode assembly fabrication with platinum-nickel nanowire catalysts." *J. Electrochem. Soc.*, **165**, F238 (2018).
65. X. Tian, X. F. Lu, B. Y. Xia, X. W. Lou, and David, "Advanced electrocatalysts for the oxygen reduction reaction in energy conversion technologies." *Joule*, **4**, 45 (2020).
66. Y. Sun, S. Polani, F. Luo, S. Ott, P. Strasser, and F. Dionigi, "Advancements in cathode catalyst and cathode layer design for proton exchange membrane fuel cells." *Nat. Commun.*, **12**, 5984 (2021).
67. J. Huang, Y. Gao, J. Luo, S. Wang, C. Li, S. Chen, and J. Zhang, "Choice—review—impedance response of porous electrodes: theoretical framework." *Physical Models and Applications. J. Electrochem. Soc.*, **167**, 166503 (2020).
68. A. Lasia, "Impedance of porous electrodes." *J. Electroanal. Chem.*, **397**, 27 (1995).
69. J. S. Newman and C. W. Tobias, "Theoretical analysis of current distribution in porous electrodes." *J. Electrochem. Soc.*, **109**, 1183 (1962).
70. R. de Levie, "On porous electrodes in electrolyte solutions: I. capacitance effects." *Electrochim. Acta*, **8**, 751 (1963).
71. C. Helbig, A. M. Bradshaw, L. Wietschel, A. Thorenz, and A. Tuma, "Supply risks associated with lithium-ion battery materials." *J. Clean. Prod.*, **172**, 274 (2018).
72. D. Schrijvers et al., "A review of methods and data to determine raw material criticality." *Resour. Conserv. Recycl.*, **155**, 104617 (2020).
73. B. Buijs, H. Sievers, and L. A. Tercero Espinoza, "Limits to the critical raw materials approach." *Proc. Inst. Civ. Eng. - Waste Resour. Manag.*, **165**, 201 (2012).